PHYSICAL REVIEW B **85**, 054110 (2012)

Effect of temperature and thermal history on borosilicate glass structure

Frédéric Angeli,[1,*] Olivier Villain,[2] Sophie Schuller,[3] Thibault Charpentier,[2] Dominique de Ligny,[4]
Lena Bressel,[4] and Lothar Wondraczek[5]
[1]*CEA, DEN, Laboratoire d' étude du Comportement à Long Terme, 30207 Bagnols-sur-Cèze, France*
[2]*CEA, IRAMIS, Laboratoire de Structure et Dynamique par Résonance Magnétique, UMR CEA/CNRS 3299, 91191 Gif-sur-Yvette, France*
[3]*CEA, DEN, Laboratoire d' étude et Développement des Matrices de Confinement, 30207 Bagnols-sur-Cèze, France*
[4]*Université de Lyon, Université Lyon 1, CNRS, UMR5620, Laboratoire de Physico-Chimie des Matériaux Luminescents,
F-69622 Villeurbanne, France*
[5]*Department of Material Science, Glass and Ceramics-WW3, University of Erlangen-Nuremberg, 91058 Erlangen, Germany*

(Received 28 September 2011; published 14 February 2012)

The influence of the temperature and quenching rate on the structure of a borosilicate glass was studied by high-resolution solid-state ^{11}B, ^{23}Na, ^{29}Si nuclear magnetic resonance (NMR) and high-temperature Raman spectroscopy. Data were obtained for glass in the solid state after annealing and quenching at cooling rates covering four orders of magnitude as well as in the liquid state from Raman experiments and from calorimetry and rheological data. Nuclear magnetic resonance measurements were used to calibrate the Raman spectra in order to quantify the change in boron coordination with temperature. This result can then be used to determine the fictive temperature of the glass directly from the boron coordination. The fictive temperature, heat capacity, and configurational entropy are extracted from calorimetry and viscosity measurements. Changes in the boron coordination account for only 25% of the configurational heat capacity of the liquid. The structural parameters capable of accounting for the remaining quantity are discussed on the basis of structural data, both local (inhomogeneity of the sodium distribution) and medium-range (from NMR parameter distribution). It has thus been shown that, although the B-O-B angular distributions of the boroxol rings (and probably the Si-O-Si distributions) are not affected by temperature, a structural disorder is identified through the angular distributions of the bonds linking borate and silicate groups.

DOI: 10.1103/PhysRevB.85.054110 PACS number(s): 61.43.Fs, 76.60.−k, 82.80.Gk

I. INTRODUCTION

Sodium borosilicate glass is a simple system underlying many industrial applications, including a large part of the waste containment glasses developed for spent nuclear fuel.[1] To avoid the formation of heterogeneities that could be detrimental to the properties of the glass matrix (viscosity, resistance to self irradiation, chemical durability, etc.), it is important to follow the melt structural evolution with temperature. Structural transformations above the glass transition temperature (T_g) can provide a better understanding of the mechanisms responsible for the liquid instability (liquid-liquid phase separation and crystallization in particular) arising from the presence of low-solubility elements, such as the rare earth elements or molybdenum in nuclear glass.[2]

Above T_g, the melt is characterized by major variations of second-order thermodynamic properties, such as heat capacity, thermal expansion, and compressibility, which can be related to configurational[3] structural changes that are still poorly known. The heat capacity of the glass is associated with atomic displacements around its equilibrium position (vibrational contribution) below T_g. At T_g, an additional contribution attributed to the distribution of atom positions appears and substantially increases with the temperature. In borates, borosilicates, or aluminoborosilicates, a decrease in tetrahedral boron with increasing quenching rates is clearly observed by nuclear magnetic resonance (NMR),[4–10] neutron diffraction,[11–13] or Raman spectroscopy.[13–16] These changes in the coordination number can represent a significant contribution to the configurational heat capacity, especially in borate glass.[7,12,13] The decrease in tetrahedral boron entails an increase in nonbridging oxygens (NBOs) that was directly confirmed by ^{17}O magic-angle spinning (MAS) NMR.[6] In borosilicate glass, the configurational contribution related to the change in boron speciation is smaller,[17] and the other structural parameters involved are not clearly established.

Numerous structural data have been acquired for sodium borosilicate glass; changes in the polymerization of the silicate network and in the ratio between tri- and tetracoordinate boron are well known according to the amount of alkalis, which can act either as charge compensators for tetrahedral boron or as network modifiers near NBOs.[18–21] Quantitative monitoring of these structural transformations is more difficult in the melt than in the solid. Nevertheless, the room-temperature glass structure already provides valuable information because it is closely related to its thermal history through the configuration acquired by the liquid when quenched. The temperature at which the glass configuration would correspond to the equilibrium configuration of the supercooled liquid, known as the fictive temperature (T_f), can vary over a range of about 200 K and is inversely proportional to the quenching rate.[22] It can be specifically imposed by annealing the glass within a narrow temperature range for which the relaxation times are not too long. It can also be studied over a broader temperature range by quenching the material at different rates.

We propose in this paper to correlate the data obtained in the solid and liquid states by coupling structural and thermodynamic approaches. A sodium borosilicate glass containing cesium was used as a nuclear glass composition model.[1] It constitutes a basic system before subsequently adding low-solubility elements (rare earth elements and molybdenum). Various heat treatments were applied, from annealing to

1098-0121/2012/85(5)/054110(15)

rapid quenching. Fictive temperatures were estimated from differential scanning calorimetry (DSC) measurements. A series of structural analysis (high-resolution solid-state NMR and high-temperature Raman spectroscopies) were coupled with calorimetric and rheological measurements.

Monitoring at high temperatures is easier to follow by Raman spectroscopy. We propose an approach capable of obtaining a very large number of measurement points during the temperature rise or fall. It is then possible to accurately monitor the evolution of structural groups, such as polymerization of the borosilicate network or the boron coordination. Quantification is still very difficult, however, and requires the use of an additional technique to calibrate the Raman spectra. ^{11}B MAS NMR was directly used to monitor the decrease in tetrahedral boron vs the temperature and, subsequently, to determine the fictive temperature corresponding to a given structural configuration.

Beyond the conventional information on coordination numbers given by ^{11}B MAS NMR, we illustrate how more detailed structural data can be obtained. First, it is shown how the NMR parameter distribution (arising from the structural disorder) can be determined from the analysis of the two-dimensional ^{11}B multiple quantum magic-angle spinning (MQMAS) spectrum. With the obtained constraints, this procedure allows the tri- and tetracoordinate borate sites to be clearly assigned in the MAS spectra. Secondly, the NMR parameter distribution extracted in this way can be interpreted in terms of structural parameters as provided by the combination of molecular dynamics simulations with first-principles calculations of NMR parameters.[23–27] Here, ^{23}Na and ^{29}Si MAS NMR are also used to complement our structural data. These results can then be discussed in light of the thermodynamic data.

II. EXPERIMENTAL

A. Sample preparation

Glass samples were prepared from powder mixtures of SiO_2, H_3BO_3, Na_2CO_3, and Cs_2CO_3 and melted in a platinum-gold crucible for 3 h at 1300 °C then poured and remelted. All the glass samples had the same nominal molar composition ($63SiO_2$-$17B_2O_3$-$17Na_2O$-$3Cs_2O$). Glass composition was checked by inductively coupled plasma atomic emission spectrometry (ICP-AES) after glass dissolution; the molar concentration was within 0.5% of the nominal composition. They were quenched by several processes to obtain various quenching rates: cooled on a plate (CP) or blown with compressed air at 1100 °C (B-1100) and 1200 °C (B-1200), forming glass fibers. Two samples were also annealed at 863 K for 1 and 100 h. The resulting glass rods were then crushed and ground in a planetary ball mill. All calculations were made using the analyzed composition; the molecular weight was taken at 68.8 g mol^{-1} and the elemental composition at 3.33 g atom mol^{-1}.

B. NMR spectroscopy

1. ^{11}B MAS and MQMAS NMR

Boron spectra were acquired at two magnetic fields 11.7 and 17.6 T. For MAS experiments, a short pulse ($\pi/12$ with a pulse width of 1 μs) was used to obtain quantitative spectra[28] with a spinning frequency of 12.5 kHz (4-mm rotor) and a repetition time of 2 s at 11.7 T and 20.0 kHz (3.2-mm rotor) and 4 s at 17.6 T. Lengthening of the spin-lattice relaxation was observed with the magnetic field increasing. To obtain constraints on the NMR parameters (as described by distributions, see below), additional 2D MQMAS experiments were carried out on certain representative samples at 11.7 T: triple-quantum MQMAS spectra optimized for the observation of either tetrahedral boron or trihedral boron. In the first case, a Z-filter pulse sequence[29] was used, and in the second case, a two-pulse sequence[30] with a rotation induced adiabatic coherence transfer (RIACT)[31] was found to yield the best signal-to-noise ratio for BO_3 species. The detailed experimental parameters have been indicated elsewhere.[32] Chemical shifts are referenced to an external sample of 1 M boric acid solution (19.6 ppm).

2. ^{23}Na MAS NMR

The sodium MAS spectra were acquired at 11.7 T with a spinning frequency of 12.5 kHz. A 1-s recycle delay and a short 1-μs pulse length ($\pi/12$) were used to obtain quantitative spectra for ^{23}Na. The external frequency reference was a 1 M NaCl solution. Additional static spectra (i.e. with a nonspinning sample) were collected at 7.05 T to measure spin-lattice relaxation times (using an inversion-recovery pulse sequence) and spin-echo decay times (or spin-spin relaxation time) for each sample.

3. ^{29}Si MAS NMR

The silicon spectra were collected at 11.7 T using a Carr–Purcell–Meiboom–Gill (CPMG) pulse sequence[33] and a 200-s recycle delay (typically 32 echoes were collected with an interpulse delay of 2 ms). Echoes were summed before Fourier transform. Spectra were referenced to an external tetrakis(trimethylsilyl)silane (TKS) sample for which the highest-intensity peak is situated 9.9 ppm from that of tetramethylsilane (TMS).

4. Theoretical analysis of the ^{11}B NMR spectra

We provide here a brief overview of the method we introduce to account for the distribution of NMR parameters for the analysis of the NMR spectra of a quadrupolar nucleus ($I > 1/2$). Under MAS, the NMR spectrum is characterized by three parameters: the isotropic chemical shift δ_{iso}, the quadrupolar coupling constant C_Q, and the quadrupolar asymmetry parameter η. The two latter parameters characterize the quadrupolar interaction, which is generally of the order of several hundreds of kHz to several MHz for ^{11}B and has therefore to be considered up to the second order (and ^{23}Na as well). The central transition ($-1/2$, $+1/2$) is generally the easiest to observe because not subjected to first-order quadrupolar interaction. Under MAS and for a crystalline compound, the NMR spectrum of the central transition displays a second-order quadrupolar line shape with well-defined singularities (see left panel, Fig. 1). In the case of a disordered system, such singularities are generally not observed because the structural disorder results in a distribution of NMR parameters, which broaden the lines, as shown in Fig. 1 (left panel). A simple procedure, widely applied to analyze

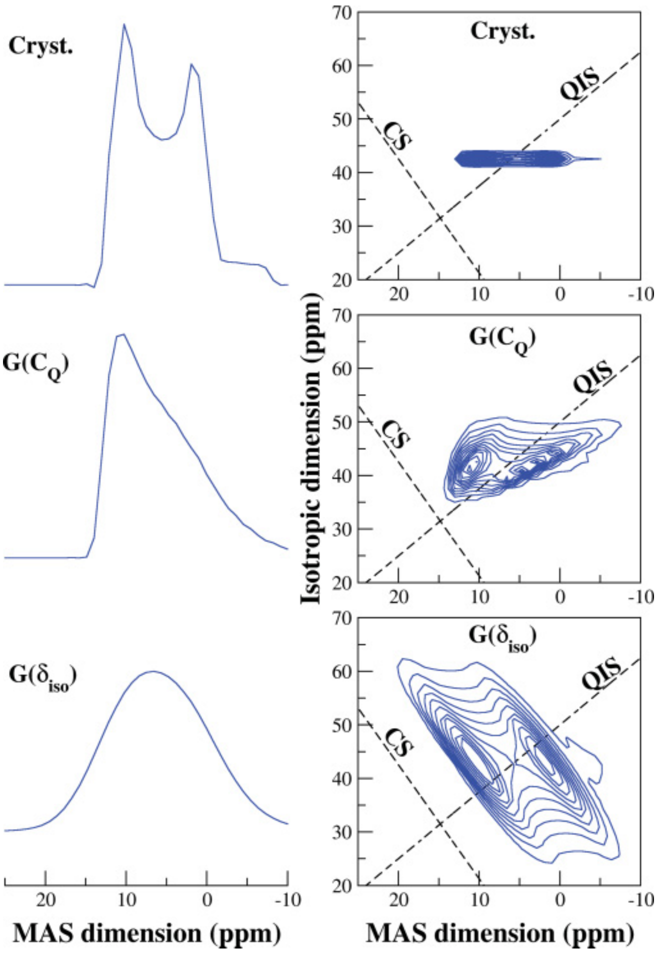

FIG. 1. (Color online) Simulated MAS (left panel) and MQMAS spectra (right) showing the effect of distributed NMR parameter ($I = 3/2$, $B_o = 11.75$ T, mean values $C_Q = 2.5$ MHz, $\delta_{\text{iso}} = 15$ ppm, and $\eta = 0.2$). Here, $G(C_Q)$ [$G(\delta_{\text{iso}})$, respectively] is a Gaussian distribution of C_Q (δ_{iso}, respectively) with a standard deviation of 0.4 MHz (4 ppm, respectively). In the right panel, dashed lines represent the direction of broadening as induced by a distribution of isotropic chemical shift (CS) and quadrupolar coupling constant (QIS).

^{11}B MAS NMR spectra of glasses, consists in considering a second-order quadrupolar spectrum broadened by a Gaussian for each site. The quadrupolar spectrum is simulated assuming a single value of the NMR parameter triplet (which can be seen as the mean value), and the Gaussian accounts (globally) for the effect of their distribution. Such a procedure generally provides satisfactory results for MAS NMR but fails when simulating the MQMAS spectrum.

A more accurate approach would require the construction of the full three-dimensional NMR parameter distribution $p(\delta_{\text{iso}}, C_Q, \eta_Q)$, which is by far too difficult from one-dimensional data. We have shown recently that two-dimensional MQMAS spectroscopy (which correlates the triple-quantum transition to the central transition) allows one to reconstruct the ^{11}B NMR parameter distribution. Indeed, as shown in Fig. 1 (right panel), the broadening induced by the distribution of isotropic chemical shift or quadrupolar interaction can be separated well. The use of distribution was shown to yield an improved analysis of the MAS spectra, which could be simulated well at multiple fields.[26] In this paper, it was demonstrated that satisfactory results were obtained using the following models:

$$\text{For} \quad \text{BO}_4: p(\delta_{\text{iso}}, C_Q, \eta) = G(\delta_{\text{iso}}) P_{\text{GIM}}(C_Q, \eta), \tag{1}$$

$$\text{For} \quad \text{BO}_3: p(\delta_{\text{iso}}, C_Q, \eta) = G(\delta_{\text{iso}}) G(C_Q) G(\eta), \tag{2}$$

where $G(x)$ is the normal (Gaussian) distribution:

$$G(x) = \frac{1}{\sqrt{2\pi}\sigma_x} \exp\left\{-\frac{(x-\bar{x})^2}{2\sigma_x^2}\right\}, \tag{3}$$

and $P_{\text{GIM}}(C_Q, \eta)$ is the Gaussian isotropic model (GIM) for the quadrupolar interaction:[34,35]

$$P_{\text{GIM}}(C_Q, \eta) = \frac{1}{\sqrt{2\pi}\sigma_Q^5} C_Q^4 \eta \left(1 - \frac{\eta^2}{9}\right) \exp\left\{-\frac{C_Q^2\left(1+\frac{\eta^2}{3}\right)}{2\sigma_Q^2}\right\}. \tag{4}$$

A crucial point to speed up the fitting procedure is the use of precalculated spectra: from $p(\delta_{\text{iso}}, C_Q, \eta)$, only a matrix-matrix (for MQMAS) or matrix-vector (for MAS) product is needed. For BO$_4$, the GIM model being parameterized by a single parameter (σ_Q), there are three adjustable parameters. From the knowledge of the distribution, the mean and standard deviation values can be calculated and are reported below. It is worth noting that, for the GIM model, the quadrupolar parameter distribution is almost independent on σ_Q (mean value 0.6 and standard deviation value 0.3). For BO$_3$, the six adjustable parameters are directly reported (they are the mean and standard deviation, respectively).

The same analysis was applied for ^{23}Na MAS NMR spectra using Eq. (4), yielding the mean value of the quadrupolar coupling constant and isotropic chemical shift.

In order to extract structural information from the NMR parameter distribution, we have applied to the ^{11}B isotropic chemical shift distribution the procedure described in Refs. 24 and 25.

C. Raman spectroscopy

For Raman measurements, the thinnest fibers of the samples B-1100 and B-1200 were chosen to recover the fibers which were cooled the fastest. Several measurements on different fibers were done. The other samples (A and CP) were investigated in their block shape. Each sample was investigated with an XPLORA confocal Raman microspectrometer by Horiba with a laser excitation at 532 nm. The Rayleigh diffusion was subtracted using an edge filter cutting at 150 cm^{-1}. The Raman signal was collected on a CCD detector with a spectral resolution of 1.8 cm^{-1} per pixel. High-temperature measurements were performed using a Linkam heating stage not higher than 1070 K to prevent any boron loss. Constant heating rate of 0.033 K s was mainly used. Spectra was acquired with an integration time of 180 s at room temperature and 75 s during dynamic heating to ensure a good signal-to-noise ratio, even between 1200 and 1600 cm^{-1}, where threefold coordinated boron presents vibrational contribution. The Raman cross sections of the Q^n species are taken arbitrarily to unity to stay as close as possible to experimental data. All spectra have been corrected regarding temperature [Eq. (5)] and baseline (4 points between 200 and 1600 cm^{-1}) and have been normalized on the silicate vibrational bands in the range of 825–1250 cm^{-1}.

$$I_{\mathrm{corr}}(\nu) = I(\nu)\tilde{\nu}_0^3\tilde{\nu}[(\tilde{\nu}_0 - \tilde{\nu})^{-4}(1 - e^{-hc\tilde{\nu}/k_BT})], \qquad (5)$$

where ν_0 is the wave number of the incident laser light and ν is the Raman shift in cm^{-1}.

D. Differential scanning calorimetry (DSC)

The fictive temperature and heat capacity were measured with a differential scanning calorimeter (Netzsch DSC 404 F1 Pegasus). About 28 mg of glass finely ground in a mortar were placed in a platinum crucible. The heating and cooling rates were systematically maintained at 0.33 K s^{-1}. The sample was first heated to 353 K for 10 min then to 925 K (scan 1), about 100 K above glass transition domain, for 3 min before cooling to 353 K. This cooling enables us to obtain a T_f corresponding to a cooling rate of 0.33 K s^{-1}. Then the same sample was heated again to 925 K (scan 2). The DSC signal was recorded throughout the temperature cycling. This procedure creates a known thermal history after an unknown thermal history. Before each measurement, an empty platinum crucible was heated and cooled to measure the baseline, and a calibration measurement was performed with a crucible containing 28 mg of sapphire.

E. Viscosity measurements

Rheological measurements in the 1100–1600 K temperature range were carried out with a Searle high-temperature coaxial cylinder viscometer. A Rheometric Scientific rheometer connected to a rotor controlled the rotation speed and measured the torque imposed by the molten glass contained in the crucible, which was heated at 0.083 K s^{-1}, then maintained at the measurement temperature for the time necessary for its stabilization. The liquid rheological behavior was analyzed for each test temperature, considering the shear stress (shear rate) associated with the rotor rotation speed (shear deformation). A total of 240 measurement points were acquired at increasing and decreasing rotation speeds during a 5-min period at each test temperature.

Viscosity was determined in the regime of 10^{13} to 10^9 Pa s by beam-bending viscometry (VIS 401, Bähr, Hüllhorst, Germany).[36]

III. RESULTS

A. Fictive temperature

Fictive temperature measurements were carried out by applying the method initially proposed by Yue[37] and refined by Guo,[38] based on the following equation:

$$\int_0^{\infty}(C_{p2} - C_{p1})dT = \int_{T_{f2}}^{T_{f1}}(C_{pl} - C_{pg})dT, \qquad (6)$$

where C_{p1} and C_{p2} are the heat capacities determined for the first and second temperature rise (scan 1 and 2) during DSC measurements, corresponding to T_{f1} and T_{f2}, respectively. Here, C_{pl} and C_{pg} represent the heat capacity of the liquid and the glass, and C_{pg} is extrapolated beyond T_{f2} by means of the following equation:[39]

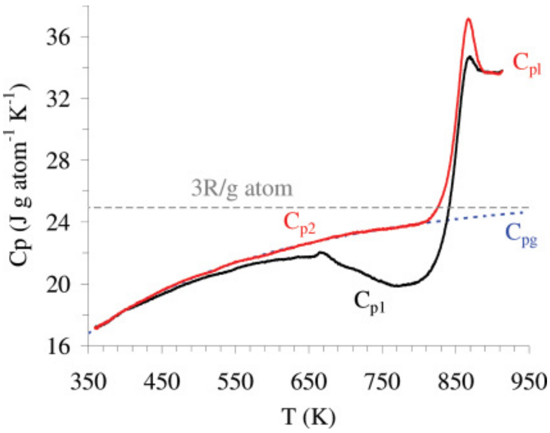

FIG. 2. (Color online) Heat capacity curves for quenched B-1100 glass measured by DSC. C_{p1} was measured during scan 1 and C_{p2} during scan 2. The cooling rate between scans 1 and 2 was 0.33 K s^{-1}. The horizontal line represents the Dulong-Petit limit.

$$C_{pg} = a + bT + \frac{c}{T^2} + \frac{d}{\sqrt{T}}, \qquad (7)$$

where C_{pg} is expressed in J g atom^{-1} K^{-1}, $a = 46.03$, $b = -4.92 \times 10^{-3}$, $c = 0.66$, and $d = -515.17$. This equation was determined in the interval 370 to 790 K with an accuracy of 1%. In the liquid state, the heat capacity was taken as a constant, $C_{pl} = 32.7 \pm 0.8$ J g atom^{-1} K^{-1} between 890 and 915 K.

Figure 2 shows the evolution of the heat capacity of glass B-1100. The glass heating and cooling rates were 0.33 K s^{-1}. Here, T_{f2} was estimated graphically at about 840 K based on the method by Yue *et al.*,[37] and T_{f1} is obtained when the areas corresponding to both terms of Eq. (6) are equal. Table I shows that the fictive temperature measured in this way ranges from 818 K (glass A) to 923 K (glass B-1200).

B. Viscosity

The viscosity measurements are indicated in Fig. 3. The most common equation used is the so-called Vogel-Fulcher-Tammann equation:

$$\log\eta = A + \frac{B}{T - T_0}. \qquad (8)$$

TABLE I. Determination of the fictive temperature by DSC and from the Raman spectra [from Fig. 13(c)]. The proportion of BO$_4$ is indicated from the values obtained at 17.6 T. The cooling rates were determined by means of Eq. (12).

	T_f (DSC) (K)	T_f (Raman) (K)	BO$_4$ (%)	Cooling rate (K s^{-1})
B-1200	923	902	70.6	798
B-1100	917	880	71.9	477
CP	857	838	74.5	1.9
SC	840			0.33
A	818	790	77.7	0.033

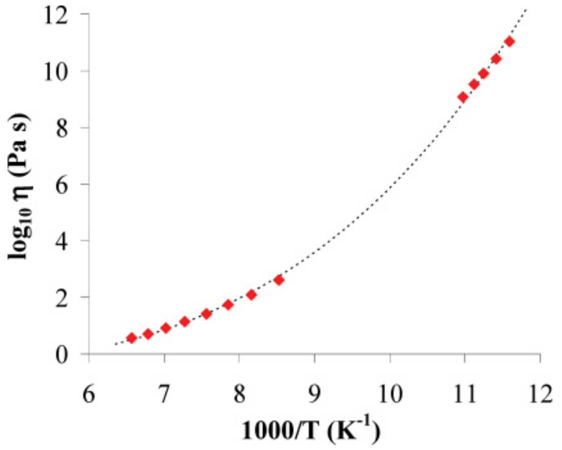

FIG. 3. (Color online) Viscosity vs temperature.

The fit with our viscosity data gives: $A = -3.36 \pm 0.46$, $B = 3339 \pm 440$, $T_0 = 636 \pm 24$. The average absolute deviation (AAD) is here 0.14.

A better fit was obtained with the following relation similar to the Avramov law,[40] formulated to satisfy the glass transition temperature definition from viscosity, i.e. at $T = T_g$: $\eta \sim 10^{12}$ Pa s.

$$\log \eta = A + (12 - A)\left(\frac{T_g}{T}\right)^{\alpha}, \tag{9}$$

where A, T_g, and α are adjustable parameters determined from the experimental data: $A = -0.70 \pm 0.18$, $T_g = 849.5 \pm 1.5$ K, and $\alpha = 4.04 \pm 0.18$. In this case, the AAD decreases at 0.08. The constant α, known as the fragility parameter (or steepness index), may be related to the fragility of the liquid.[41]

C. NMR spectroscopy

1. ^{11}*B MAS and MQMAS NMR*

The ^{11}B MAS NMR spectra are displayed in Fig. 4. Several sites are generally underlying the narrow tetrahedral boron peak near 0 ppm. A boron atom surrounded only by silicon atoms is usually found at −2 ppm,[42] and the isotropic chemical shift increases with the number of second-neighbor boron atoms.[43,44] It is difficult, however, to quantify unequivocally the sites corresponding to each of these contributions. Here, ^{11}B MQMAS NMR may resolve the contributions related to tetrahedral boron by discriminating between a boron atom surrounded by four silicon atoms [BO_4(0B, 4Si) ∼ −2 ppm] and a boron atom surrounded by three silicon atoms and one boron atom [BO_4(1B, 3Si) ∼ 0 ppm]. These two sites also differ by their mean quadrupolar coupling constant, as corroborated by detailed analysis of the spinning sidebands manifold of the satellite transitions.[26] At about 10 ppm, two other contributions are well resolved because of strong quadrupolar interactions. They can be attributed in this type of composition to tricoordinate boron, either ring type in boroxol rings or involving both BO_3 and BO_4 ($BO_{3\,\mathrm{ring}}$) or nonring type, outside the rings ($BO_{3\,\mathrm{nonring}}$).[10,44] The proportions of each of these sites is determined following a method previously described.[26]

To improve the accuracy of the quantification of the relative populations of tri- and tetracoordinate species, it is valuable to use higher magnetic fields (17.6 T in this case) that can clearly separate these two kinds of resonance. However, the second-order quadrupolar broadening of the trihedral site decreases with the magnetic field strength, making it more tricky to discriminate between the different BO_3 sites. It may therefore be preferable to use a lower field (11.7 T here). Therefore, all the glass specimens here were examined at these both complementary fields. Spectra were fitted after correction for the contribution due to satellite transitions by subtracting the first spinning sideband from the central band.[26] Comparing the fit with and without such correction shows that the satellite transitions contribute on average to 2% of the proportion of BO_4 in the central (spinning) band. At each field, spectra of all glass specimens were analyzed (fitted) using the same set of NMR parameters, allowing only the amplitudes (i.e. site population) to vary. To obtain parameter constraints and line shape models, a detailed analysis of the boron MQMAS spectra was carried out at 11.7 T (see below). The model was used to determine the NMR parameter distribution (δ_{iso}, C_Q, and asymmetry parameter η_Q). Results are gathered in Table II. A typical fit is shown for the annealed glass A in Fig. 5.

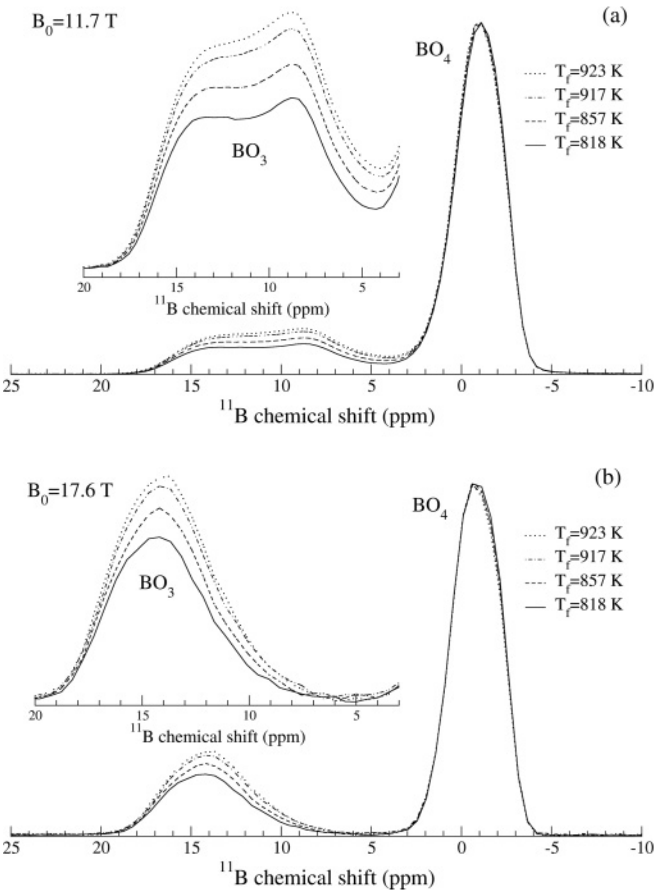

FIG. 4. The ^{11}B MAS NMR spectra of glass quenched at different rates (normalized on the maximum contribution of BO_4) under two different magnetic fields: (a) 11.7 T and (b) 17.6 T.

The ^{11}B MQMAS NMR spectra of the tetrahedral site in the experimental [Fig. 6(a)] and simulated [Fig. 6(b)] annealed glass are in good agreement. The data allowed us to implement an isotropic normal (Gaussian) distribution model of the electric field gradient characterized by a single

TABLE II. The NMR parameters obtained from MAS spectrum analysis at 11.7 and 17.6 T. A single parameter set was used to fit all the contributions at 11.7 T, then at 17.6 T.

	NMR parameters		Relative intensity				
	δ_{iso} (ppm)	C_Q (MHz)	η	A	CP	B-1100	B-1200
$B_0 = 11.7$ T							
$BO_{3\,\mathrm{ring}}$	17.9 (1.0)	2.56 (0.04)	0.3 (0.1)	13.5	14.9	16.0	16.5
$BO_{3\,\mathrm{nonring}}$	14.9 (2.3)	2.70 (0.16)	0.3 (0.1)	9.7	11.7	13.8	14.7
BO_4(1B,3Si)	0.0 (1.0)	0.58 (0.18)	0.6 (0.3)	46.9	46.1	44.7	44.4
BO_4(0B,4Si)	−1.7 (1.0)	0.19 (0.06)	0.6 (0.3)	29.9	27.3	25.6	24.4
$B_0 = 17.6$ T							
$BO_{3\,\mathrm{ring}}$	17.4 (1.0)	2.50 (0.04)	0.2 (0.1)	17.2	18.6	19.6	20.5
$BO_{3\,\mathrm{nonring}}$	15.0 (1.3)	2.70 (0.20)	0.2 (0.1)	5.2	6.9	8.5	9.0
BO_4(1B,3Si)	−0.1 (1.1)	0.58 (0.18)	0.6 (0.3)	47.9	46.5	45.0	44.8
BO_4(0B,4Si)	−1.7 (0.9)	0.19 (0.06)	0.6 (0.3)	29.8	28.0	26.9	25.8

constant σ_Q,[34,35] as described in the experimental section. This distribution was coupled with an isotropic normal chemical shift distribution.[26] Using this distribution for two sites accounts very satisfactorily for both the MAS and MQMAS spectra. The NMR parameter distribution [Fig. 6(c) and 6(d)] shows that the two sites strongly differ in their C_Q distribution [Fig. 6(c)]. The BO_4 site surrounded only by Si atoms, more symmetric than the BO_4 site surrounded by three Si and one B, logically indicates a lower C_Q distribution.

The same approach was applied to tricoordinate boron, as shown in Fig. 7. The MQMAS spectrum was deconvoluted by means of a distribution model using the product of three normal distributions (δ_{iso}, C_Q, and η_Q)[32] [Eq. (2)] with a correlation effect, as recently introduced for ^{17}O (Ref. 27) or ^{11}B in binary SiO_2-B_2O_3 glasses.[25] Two sites are sufficient to account for the entire experimental spectrum very satisfactorily. In this case, the most remarkable difference is observed for the δ_{iso} distribution [Fig. 7(c)]. The sensitivity of this interaction to the B-O-B bond angles has recently been demonstrated.[45] The boron atoms in boroxol rings ($BO_{3\,\mathrm{ring}}$) are then characterized by a narrower δ_{iso} distribution, resulting in a smaller dispersion of the B-O-B angles.

The variation in tetrahedral boron is plotted vs the glass quenching rate in Fig. 8(a). A drop of about 7% in tetrahedral boron was measured as the quenching temperature increased. This is of the same order of magnitude as the value usually observed for this type of composition.[5,8]

The quantification of these four contributions obtained at 11.7 and 17.6 T are plotted in Fig. 9. The agreement between the two fields is satisfactory. The borate sites surrounded only

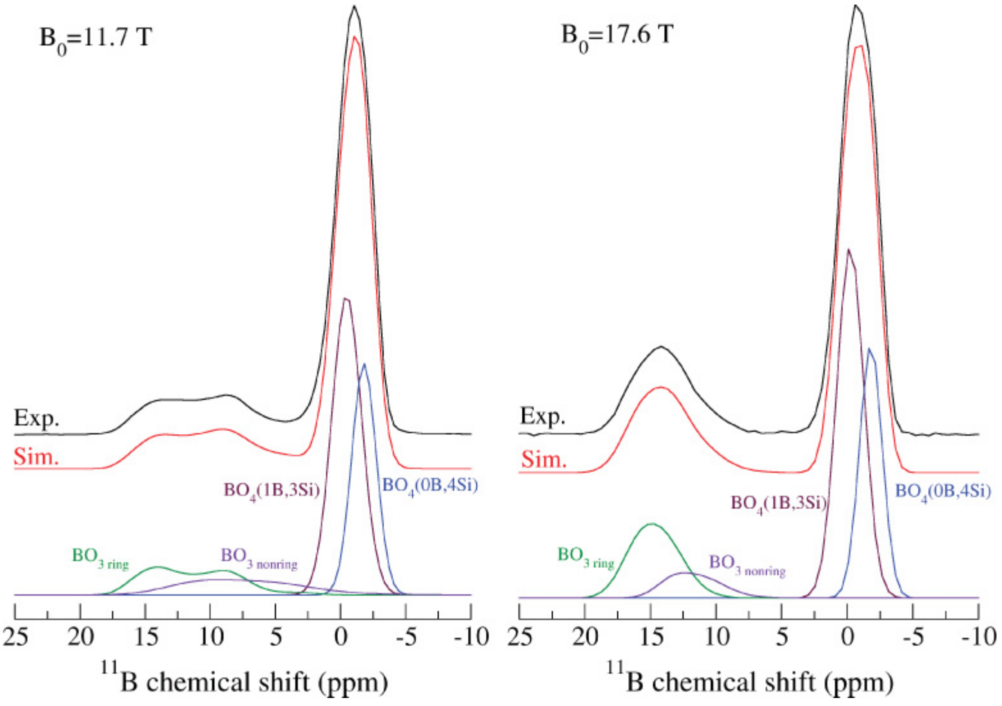

FIG. 5. (Color online) Decomposition of ^{11}B MAS NMR spectrum of glass A acquired under two different magnetic fields (11.7 and 17.6 T).

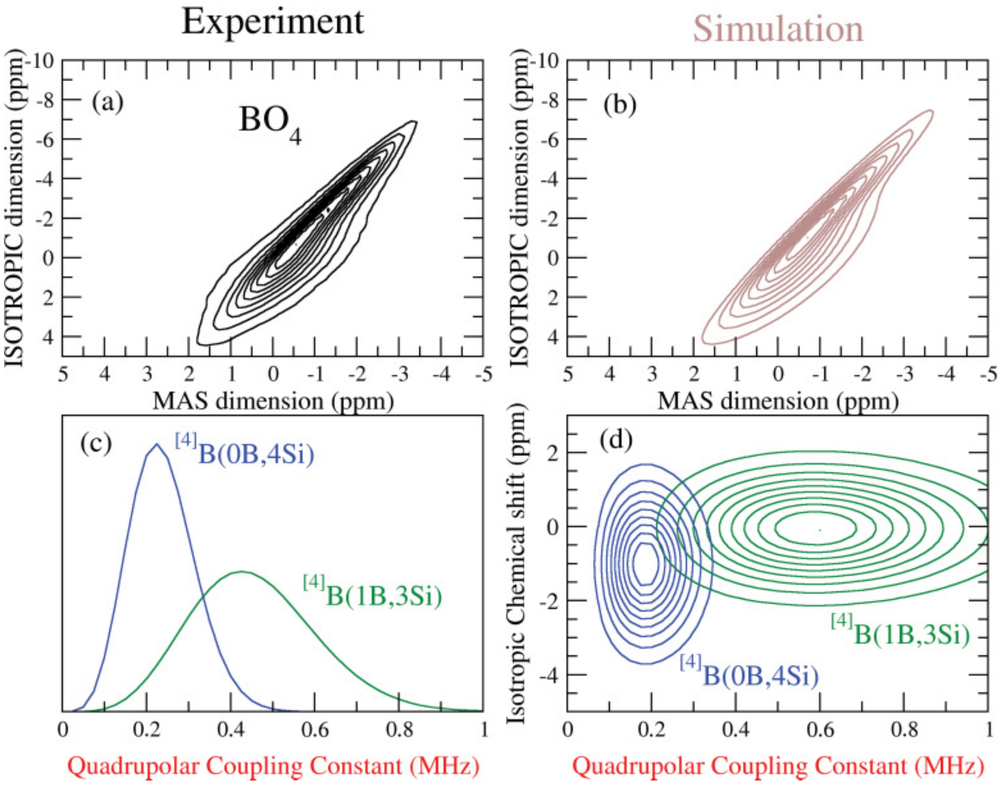

FIG. 6. (Color online) (a) Experimental and (b) simulated ^{11}B MQMAS NMR spectra of tetrahedral boron in annealed glass A, (c) distribution of quadrupolar coupling constant C_Q, and (d) distribution map (δ_{iso}, C_Q).

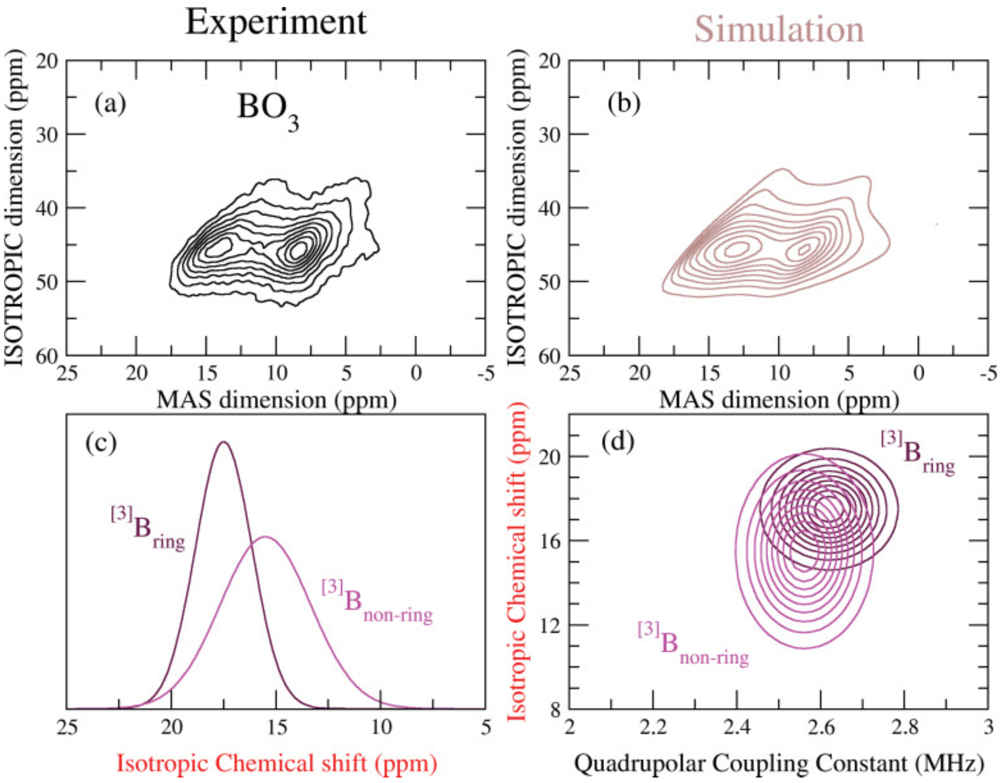

FIG. 7. (Color online) (a) Experimental and (b) simulated ^{11}B MQMAS NMR spectra of trihedral boron in annealed glass A, (c) isotropic chemical shift distribution δ_{iso}, and (d) distribution map (δ_{iso}, C_Q).

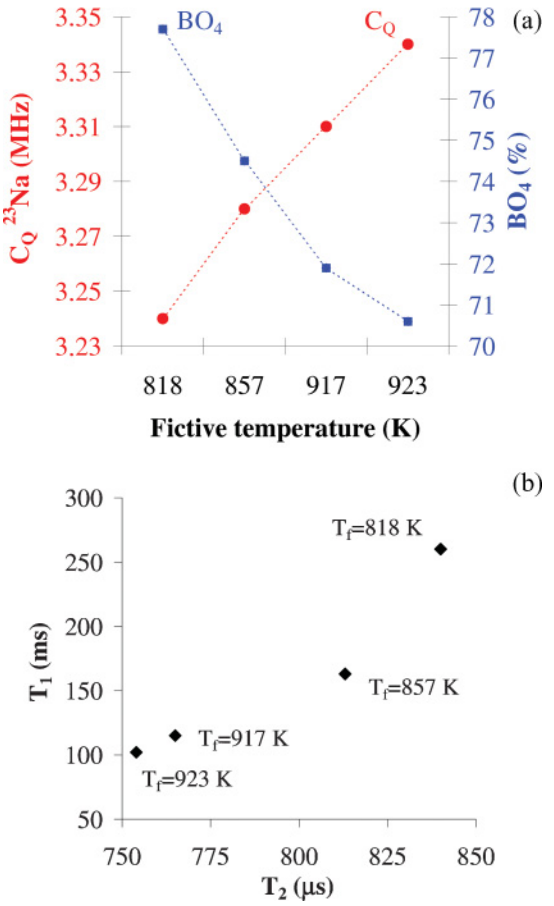

FIG. 8. (Color online) (a) Quadrupolar coupling constant C_Q of ^{23}Na and proportion of tetrahedral boron vs fictive temperature. (b) Relaxation times T_1 (ms) and T_2 (μs) of glasses.

by Si [BO_4(0B, 4Si)] seem preferentially diminished when the quenching rate increases. As discussed above, it is more difficult in strong magnetic fields to accurately determine the trihedral boron contributions, and greater confidence can be placed in the distribution of the two sites at 11.7 T. To check that annealing glass A for 1 h was sufficient for complete relaxation, a specimen was annealed again for 100 h, after which no difference was visible in the NMR or the Raman spectra.

2. ^{23}Na MAS NMR

Simulation of the ^{23}Na MAS spectra (not shown) pointed out that δ_{iso} increases only very slightly from −3.7 to −3.5 ppm when the fictive temperature increases, indicating a small decrease in the Na-O distance. Shorter Na-O bond distances result in diminished electron shielding and thus an increase in the δ_{iso} of sodium.[46–48] This effect can be related to a larger proportion of NBO-Na sites with shorter bond distances when Na acts as a boron charge compensator.[49] However, the C_Q variation of ^{23}Na is more pronounced, as shown in Fig. 8(a), where a regular increase with the quenching rate is observed.

An additional data series was obtained from ^{23}Na under static conditions (i.e. nonspinning sample) [Fig. 8(b)] by measuring the two characteristic times for the nuclear spin magnetization to reach its equilibrium value: the spin-lattice relaxation time T_1 and the spin-spin relaxation time T_2. The same effect was observed for both relaxation times: T_1 decreases from about 250 to 100 ms as the quenching rate increases, whereas T_2 decreases from about 850 to 750 μs.

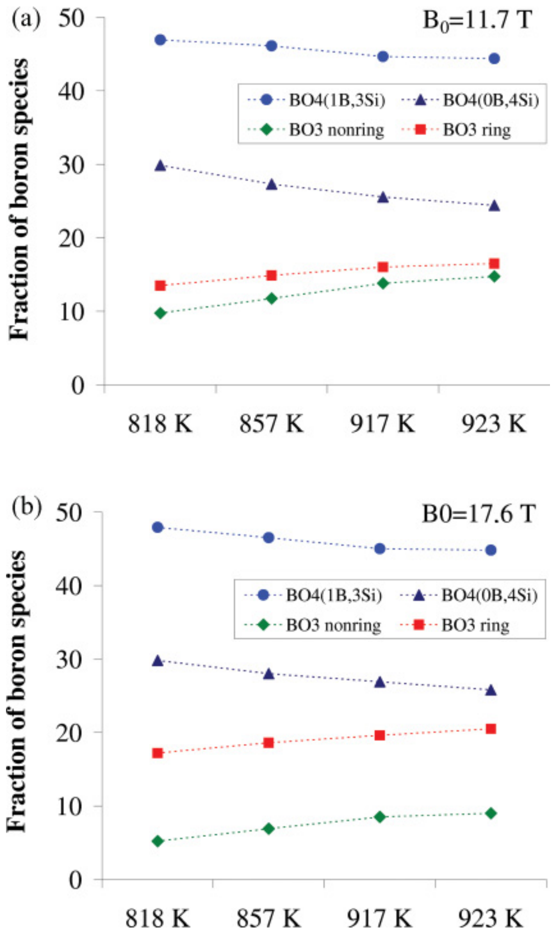

FIG. 9. (Color online) Evolution of boron speciation of glass quenched at different rates determined from ^{11}B MAS NMR spectra at (a) 11.7 T and (b) 17.6 T vs fictive temperature. Broken lines are simple visual aids.

3. ^{29}Si MAS NMR

The ^{29}Si MAS spectra (Fig. 10) are practically identical for the various heat treatments, although the number of NBO atoms varies, and thus the degree of polymerization to which ^{29}Si NMR is sensitive. The apparent lack of variation in the spectra can be related to the presence of a boron atom as a second-neighbor of a silicon atom, which shifts the lines in the opposite direction of increasing polymerization.[50] More specifically, it has also been recently suggested that the contribution at about 90 ppm in the ^{29}Si MAS spectra was more likely due to Si(Q^3) and Si(Q^4)-BO_4 units. The contribution at about 100 ppm is related to fully polymerized species Si(Q^4) and to Si(Q^4)-$BO_{3\,\text{nonring}}$ units.[25] Under these conditions, all the contributions can be calculated, and considering the shifts related to the type of second-neighbor boron atom surrounding the silicon atom, it can be shown that the line position is not modified, which is consistent with the experimental results. The two effects cancel each other with the decrease of the

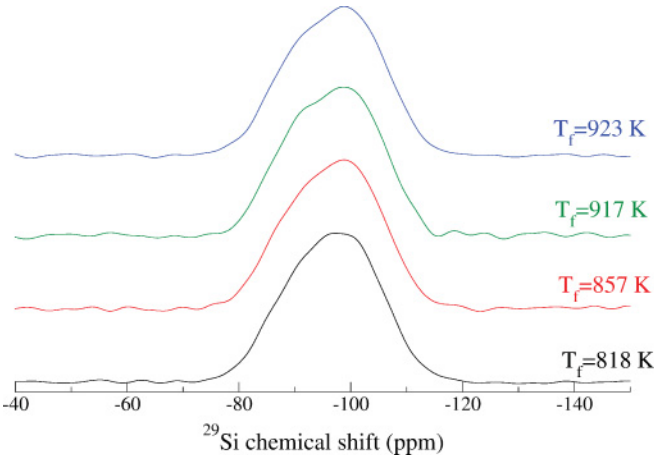

FIG. 10. (Color online) The ^{29}Si MAS NMR spectra of glass with various fictive temperature.

BO_4/BO_3 ratio: an increase in the number of NBOs, and thus of Si(Q^3) units, and a decrease in the [Si(Q^4)-BO_4] species at 90 ppm. At the same time, a decrease in Si(Q^4) units and an increase in Si(Q^4)-$BO_{3\,\mathrm{nonring}}$ units is observed at 100 ppm.

D. Raman spectroscopy

The Raman spectra were deconvoluted into 11 bands, as indicated in Fig. 11, together with the assignment of the bands related to borate species and network polymerization (Q^n). The narrow band around 630 cm^{-1} (band 2 in Fig. 11) was attributed to danburite rings,[51] i.e. tetrahedral boron, whereas most of the trihedral boron should be found around 1450 cm^{-1} (bands 9 and 10) with the B-O-B and B-O$^-$ stretching modes of the BO_3 groups.[52,53] We recently showed that these contributions are relatively well correlated with the boron coordination quantified by NMR.[26] Finally, the broad band between 830 and 1275 cm^{-1} was associated with the Si-O bond stretching modes of Q^n species represented in Fig. 11 by bands 5, 6, 7, and 8 (the most highly polymerized species correspond to the highest wave numbers).[54,55]

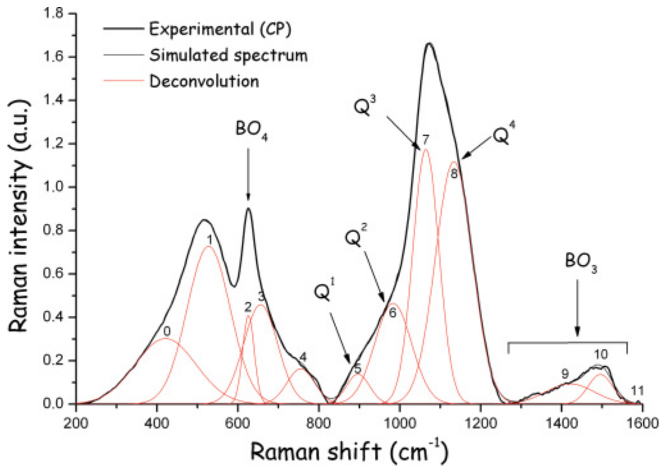

FIG. 11. (Color online) Deconvolution of Raman spectrum. This figure illustrates CP glass, but the same type of deconvolution was applied to all the glasses.

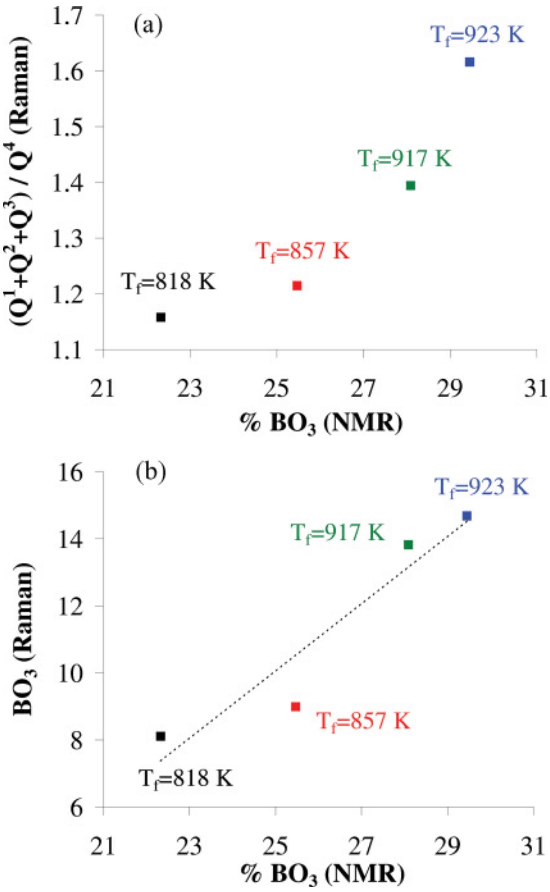

FIG. 12. (Color online) (a) Depolymerization of the network based on the ratio between the area under the Raman bands assigned to $Q^1 + Q^2 + Q^3$ over Q^4 species. (b) Area under Raman bands assigned mainly to BO_3 species vs the proportion of BO_3 measured by ^{11}B NMR.

Information on the evolution of network polymerization, which is not directly accessible by ^{29}Si NMR, as shown in the preceding section, is observed here: Fig. 12(a) shows the variation in the $(Q^1 + Q^2 + Q^3)/Q^4$ ratio according to the proportion of trihedral boron in the samples. Depolymerization clearly appears as the fictive temperature increases; it reflects the increase in NBOs when Na becomes a network modifier. The evolution of trihedral boron follows the same trend in the Raman spectra as for NMR, based on the area of the contributions around 1400–1450 cm^{-1} [Fig. 12(b)]. The correlation between the Raman data and the boron coordination quantified by NMR can then be used for quantitative monitoring of coordination number at high temperature directly from the Raman spectra.

In situ high-temperature Raman spectroscopy can thus be used to monitor the evolution of structural groups beyond the glass transition temperature and, in particular, the polymerization of the glass network and the boron speciation. These measurements were carried out on a previously annealed sample at temperatures up to 1073 K with a heating rate of 0.033 K s. Other heating rates up to 0.42 K s were tested with no significant differences. The 0.033 K s spectra were selected because of the better signal-to-noise ratio. The samples were heated to 1073 K and quenched always at the

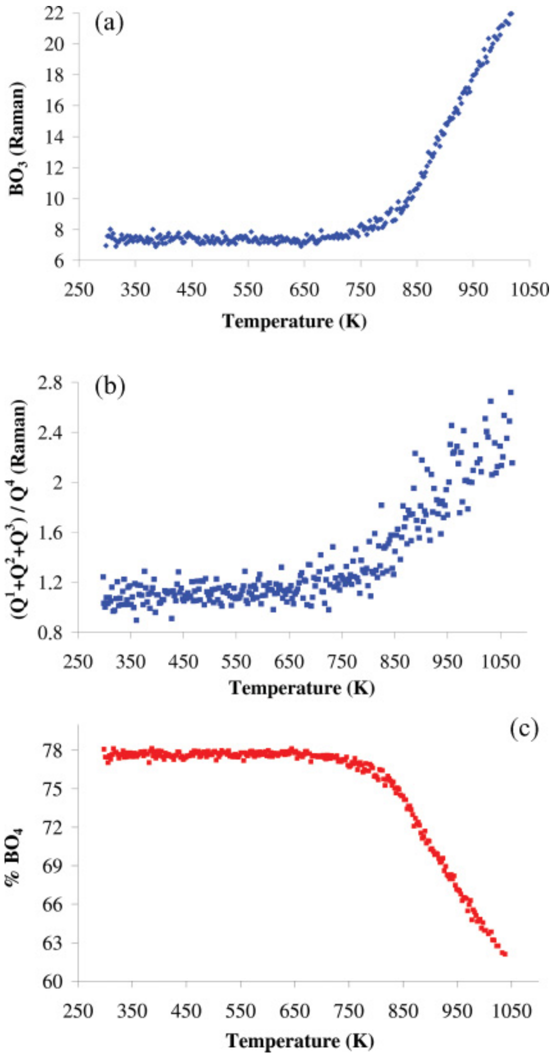

FIG. 13. (Color online) (a) Area of Raman bands assigned mainly to BO_3 and (b) $(Q^1 + Q^2 + Q^3)/Q^4$ ratio vs temperature. (c) Tetrahedral boron percentage vs temperature estimated by Raman calibration of NMR data.

same rate with very good reversibility. For greater clarity, only the data corresponding to the temperature rise are shown here.

Figure 13 compares the variation with the temperature in the area of the Raman bands mainly attributed to 3-coordinate boron [Fig. 13(a)] and the depolymerization of the network through the $(Q^1 + Q^2 + Q^3)/Q^4$ ratio [Fig. 13(b)]. Although the latter contribution is relatively noisy, the variations in the boron coordination and polymerization appear to be correlated; sodium which no longer compensates boron adopts a network-modifying position and increases the number of NBO atoms.

IV. DISCUSSION

The complementarity of NMR and Raman spectroscopy is clearly pointed out in this study. Raman spectra provide information on the degree of polymerization that cannot be obtained by ^{29}Si NMR, which chemical shifts are sensitive to the nature of the second neighbor around the silicon atom. The Raman spectra clearly show the depolymerization of the silicate network with the quenching rate increasing. This confirms that most of the NBOs are linked to silicon rather than boron atoms. The decrease in polymerization with increasing temperature can thus be ascribed to the diminishing population of tetrahedral boron species.

Quantification at room temperature of boron speciation from ^{11}B MAS NMR can then be used to calibrate the Raman data, as shown by the correlation of the NMR data with the Raman BO_3 bands displayed in Fig. 12(b). Evolution of the fraction of tetrahedral boron, as measured from Raman at variable temperature, can then be obtained, as shown in Fig. 13(c). In the temperature range investigated, the boron speciation can then be estimated at a given temperature. Conversely, this type of figure can be used to estimate T_f graphically if the proportion of tetrahedral boron is known. Good agreement is obtained between T_f determined in this way by Raman spectroscopy and by DSC. For example, for the highest quenching rate $T_{f\text{-Raman}} = 902 \pm 8$ K and $T_{f\text{-DSC}} = 923 \pm 20$ K (Table I). The T_f interval investigated here extends over a range of 105 K for variations of about 7% in the boron coordination.

It is important to note that the transition from high to low temperature appears here to be gradual, whereas it should normally occur suddenly when the system freezes during quenching. This effect should be related to the slow system relaxation time when compared with the Raman measurement time, which was typically 75 s. Viscosity measurement may provide an answer here.

A significant deviation from Arrhenius behavior can be observed in Fig. 3 due to structural changes that occur in the liquid state.[3,56,57] Only the linear part in the low-temperature range is taken into account to estimate the relaxation time τ from the Maxwell relation:

$$\tau = \frac{\eta}{G_0}, \tag{10}$$

where G_0 is the shear modulus, about 2.5×10^{10} Pa for this type of composition.[58]

The estimated temperature for a relaxation time of 75 s (corresponding to the time of the Raman measurement) is 831 K. By lowering the temperature, the measured values begin to deviate from the melt line in Fig. 13(c) for this temperature until the glass line around 745 K. In the temperature range 745–831 K, the relaxation time of the glass interferes with the Raman measurement time. Raman data should therefore only be used in the linear high-temperature range corresponding to the fully relaxed regime. In this regime, a structural relaxation activation energy E_a can be estimated from the following relation:

$$\eta = \eta_0 \exp\left(\frac{E_a}{RT}\right). \tag{11}$$

An E_a value of 605 kJ mol^{-1} is obtained, in good agreement with data for aluminoborosilicates estimated from DSC measurements between 560 and 726 kJ mol^{-1}.[10] This activation energy obtained near T_g can be used to determine the dependence of T_f on the glass quenching rate; the similarities between the rearrangements that occur during structural relaxation and during viscous flow allow the activation energy (E_a) of viscous flow to be equated with that of structural relaxation (Δh^*).[22,59] It is then possible to determine glass quenching rates (q_2) from the T_f value (T_{f2}) as well as that of a reference glass prepared with a known quenching rate and measured fictive temperature ($q_1 = 0.33$ K s, $T_{f1} = 840$ K):

$$\frac{\ln q_1 - \ln q_2}{\frac{1}{T_{f_1}} - \frac{1}{T_{f_2}}} = -\frac{\Delta h^*}{R}. \tag{12}$$

The quenching rates obtained in this way are indicated in Table I together with the glass used as the reference quenching rate at 0.33 K s (designated SC for slow cooling). A variation of four orders of magnitude in the quenching rate, from 0.033 to 798 K s^{-1}, results in the variation in the fictive temperature of 105 K.

Adam-Gibbs relaxation theory[60] suggests that the relaxation time of a property of the liquid is inversely proportional to the probability of a rearrangement of its structure. Under these conditions, mass transfer in a viscous liquid requires a cooperative change in the liquid configuration. Viscous flow can thus be related to the configurational entropy $S^{\text{conf}}(T)$ of the liquid at temperature T:[56]

$$\log \eta = A_e + \frac{B_e}{T\, S^{\text{conf}}(T)}. \tag{13}$$

Here, A_e is a pre-exponential term and B_e is a constant proportional to the Gibbs free energy barrier opposing the configurational rearrangement required for viscous flow. These constants are temperature independent and vary with the glass composition. The configuration entropy can be split into a chemical configuration entropy that accounts for the distribution of elements on similar sites, and a structural configuration entropy determined by topological parameters. Here, $S^{\text{conf}}(T)$ can be estimated from the viscosity curves or from the quantification of structural groups that vary with the temperature.[61] It can be calculated from heat capacity measurements as follows:

$$S^{\text{conf}}(T) = S^{\text{conf}}(T_g) + \int_{T_g}^{T} \frac{C_p^{\text{conf}}}{T} dT, \tag{14}$$

where $S^{\text{conf}}(T_g)$ is the configurational entropy at the glass transition temperature, and $C_p^{\text{conf}}(T)$ is the configurational heat capacity of the liquid. The latter can be considered equal to the difference between the heat capacity of the liquid [$C_{pl}(T)$] and the vibrational heat capacity, which can be estimated for silicates from the C_p of glass at T_g [$C_{pg}(T_g)$]:[62]

$$C_p^{\text{conf}}(T) = C_{pl}(T) - C_{pg}(T_g). \tag{15}$$

Near T_g, the heat capacity of the glass [$C_{pg}(T_g)$] tends toward the Dulong-Petit limit ($3R$/g atom, where R is the gas constant). Considering the T_g value determined by DSC [estimated from T_{f2} in Eq. (12)] of 840 K, the $C_{pg}(T_g)$ value of 24.1 ± 0.2 J g atom^{-1} K^{-1} (Fig. 2) is very near (97%) the Dulong-Petit limit. By similarly inferring the [$C_{pl}(T)$] value of 32.7 J g atom^{-1} K^{-1}, the configurational heat capacity of the liquid is thus $C_p^{\text{conf}}(T) = 8.6$ J g atom^{-1} K^{-1}, in agreement with data for sodium borosilicate glasses ranging from 5 to 10 J g atom^{-1} K^{-1}.[63]

In ternary sodium borosilicate glasses, which compositions are near to the one of the glass studied here, it has been shown that the heat capacity in the liquid is independent of the temperature.[64] The evolution of the configurational entropy can therefore be calculated as a function of temperature from Eqs. (13)–(15) based on calorimetry and viscosity data and assuming $C_p^{\text{conf}}(T)$ is constant. The coefficients of Eq. (13) are $A_e = -2.53$ and $B_e = 1.18 \times 10^5$. The value obtained at T_g for $S^{\text{conf}}(T_g)$ is 2.7 ± 0.4 J g atom^{-1} K^{-1}, with AAD = 0.14. The configurational entropy is thus of the same order of magnitude than the data obtained for other sodium borosilicates.[63–65] The low cesium concentration in our glasses does not appear to have a significant effect on the value of $S^{\text{conf}}(T_g)$. With more complex glass compositions, the comparison of the configurational entropies will allow us to discuss the influence of adding particular elements on the overall disorder of the glass matrix.

In borosilicate glass, a major source of configurational entropy around the glass transition range may be associated with the borate network.[7,12,13,66] The contribution of boron speciation to the change in configurational heat capacity $\left(C_p^{\text{conf}}\right)$ can be calculated from the apparent equilibrium constant K of the reaction of the boron coordination change, $BO_4 \leftrightarrow BO_3 + \text{NBO}$:[5]

$$K = C\left[\frac{C_{\text{NBO}} C_{\text{BO}_3}}{C_{\text{BO}_4}}\right], \tag{16}$$

in which C is the factor corresponding to the concentration ratios, which is assumed not to depend on the temperature. The BO_3 and BO_4 concentrations (designated C_{BO3} and C_{BO4}, respectively) are determined from NMR measurements, whereas the NBO concentration is calculated by assuming that all the Na not compensating BO_4 groups are the source of Si-NBOs.

Given the quantification of structural groups at two different temperatures and assuming that the activity coefficient of this reaction is temperature independent, the enthalpy of the speciation change reaction can be estimated with the van't Hoff relation:

$$\Delta H = -R\frac{\ln K_1 - \ln K_2}{\left(\frac{1}{T_{f1}}\right) - \left(\frac{1}{T_{f2}}\right)}. \tag{17}$$

For the two extreme fictive temperatures (818 and 923 K), Eq. (17) gives $\Delta H = 34$ kJ mol^{-1}. With a sodium borosilicate glass ($60SiO_2$-$20B_2O_3$-$20Na_2O$), for a T_f amplitude of 100 K, Sen *et al.*[8] obtained a similar variation of the boron coordination, resulting in enthalpy values of the same magnitude as ours, with $\Delta H = 39$ kJ mol^{-1}. In aluminoborosilicates, this value ranges from 24 to 50 kJ mol^{-1}; it decreases with the field strength of the network-modifying cation, which diminishes the probability of compensation of tetrahedral boron (and thus of the reaction $BO_4 \leftrightarrow BO_3 + \text{NBO}$).[10]

Figure 14 shows all the experimental data points from the linear portion of the BO_4 curve in the high-temperature range [Fig. 13(c)] after recalculating the apparent equilibrium constant K for each point. The resulting straight line shows that the C factor of Eq. (16) is indeed constant and is not temperature dependent. The line slope gives $\Delta H = 32$ kJ mol^{-1}; this *in situ* high-temperature study covering a range of 220 K is thus in good agreement with the preceding value of 34 kJ

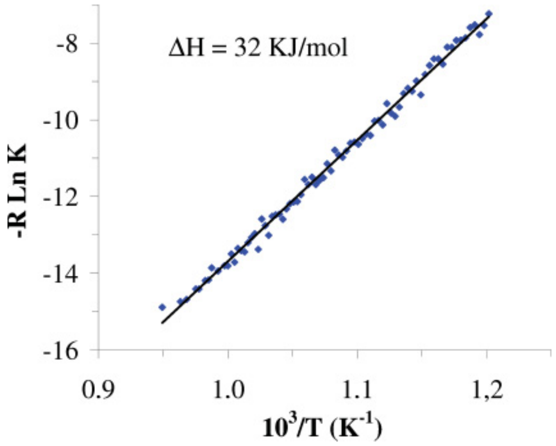

FIG. 14. (Color online) Apparent equilibrium constant K of reaction $BO_4 = BO_3 + NBO$ vs temperature. The slope of the line directly gives the enthalpy of the speciation change reaction (32 kJ mol^{-1}) based on the experimental data derived from Raman spectra.

mol^{-1} obtained for glass quenched from two separated fictive temperatures of 105 K.

It becomes then possible to estimate the contribution $C_p^{\text{conf}}(B)$ related to changes in the boron coordination ΔX and NBO (included in the calculation of the enthalpy ΔH) over a temperature range ΔT:[10]

$$C_p^{\text{conf}}(B) \approx \Delta H \frac{\Delta X}{\Delta T}. \tag{18}$$

The value obtained, $C_p^{\text{conf}}(B) = 2.1$ J g atom^{-1} K^{-1}, can be compared with the overall contribution of the configurational heat capacity of the liquid $C_p^{\text{conf}}(T)$ determined earlier ($C_p^{\text{conf}} = 8.6$ J g atom^{-1} K^{-1}). Under these conditions, changes in the boron coordination account for only about 25% of the configurational heat capacity of the liquid, contrary to the findings reported by Sen *et al.*[8] for sodium borosilicates, for which the borate speciation reaction appears to be the main contributor. However, their study did not compare C_p values between the same compositions; they calculated C_p values from the boron coordination but compared them to the total measured C_p values from prior studies.

The configurational component of boron speciation obtained in this paper is of the same order of magnitude as the values obtained for aluminoborosilicate glass, ranging from 7% to 30%.[10] This proportion generally increases with the boron concentration in the glass. It is significantly greater in binary sodium borate glasses for which the change in the boron coordination accounts almost entirely for the configurational contribution.[7,12,13] The evolution of the silicon coordination revealed by Raman spectroscopy could also contribute, but only to a limited extent; in sodium silicates, less than 30% of the configurational contribution is related to variations involving Q^n species.[17]

A large part of the configurational contribution is therefore due to other factors than changes in the boron speciation. The alkali environment can be investigated to identify other local structural contributions that can vary with the quenching rate. Here, ^{133}Cs MAS NMR (not shown) did not reveal any significant variation between glass compositions; ^{23}Na MAS NMR showed a steady increase in the quadrupolar coupling interaction as the quenching rate increased. Related to the charge distribution around the nucleus (electric field gradient) and thus to the symmetry around the Na site, it could reflect changes in the alkali coordination and/or a different cation spatial distribution. It may be related to the increasing disorder around Na sites with the quenching rate.

Further information could be obtained from ^{23}Na relaxation time measurements. The decrease in the sodium relaxation time in molten glass is typically attributed to the mobility of the nuclei.[67] In our case, there is no reason for any differences in sodium mobility between the glasses. The presence of paramagnetic impurities can also affect the relaxation time, but because the heat treatments were performed on the same glass composition, there can be no differences in the concentrations of these impurities. Nevertheless, measurements of the sodium relaxation time [Fig. 8(b)] show that the spin-spin relaxation time T_2 diminishes steadily as T_f increases (from about 850 to 750 μs), which may in this case reflect an increase in Na-Na dipolar interactions. The number of closely arranged Na atoms would therefore increase with the quenching rate: frozen in more rapidly, the system apparently leaves less time for Na to be homogeneously distributed in the network and thus favors Na clustering. The spin-lattice relaxation time T_1 decreases slightly more, from about 250 to 100 ms. Two relaxation mechanisms could explain such a variation (both reflective of change in the Na environment): fluctuations of the local electric field gradient (quadrupolar interaction)[68,69] and/or Na-Na dipolar interactions. From the apparent increase of Na-Na interactions (T_2) one could expect a more efficient dipolar relaxation mechanism (thus decreasing T_1).

On the other hand, topological parameters, such as angular distributions, may also likely affect the configurational contribution. As noted in the experimental section, the ^{11}B MQMAS NMR spectra can be used to determine the distribution of NMR parameters (more accurately than MAS), which can then be interpreted in terms of structural parameters, using relationships derived from a combination of molecular dynamics simulations and first-principles calculations.[24,25,70] Figure 15 shows the correlation between the isotropic chemical shift of three-folded ^{11}B and the mean B-O-T bond angle (where T = B or Si) obtained for borosilicate glasses.[25] The ^{11}B isotropic chemical shift distributions can therefore be expressed as B-O-T angular distributions (T = Si, B) of trigonal boron. This distribution is obtained by a fitting procedure which optimizes the agreement between experimental δ_{iso} distribution (for ring and nonring species) and the one simulated with the distribution of bond angles. The result is shown in Fig. 16 for the two glasses at the two extreme quenching rates: annealed glass (A) and the most rapidly quenched glass (B-1200).

Three contributions can clearly be distinguished. The $BO_{3\,\text{ring}}$ contribution includes a first distribution (angle α) situated around 120° because it contains the internal angles of the boroxol rings (this mean value is constrained during the fitting procedure, but not the distribution). The second contribution (angle β) comprises the external angles of the boroxol rings, which can also be bonded with silicon. Although they are linked to the rings, they are less constrained than inside the rings, and the angles of these bonds are larger, centered

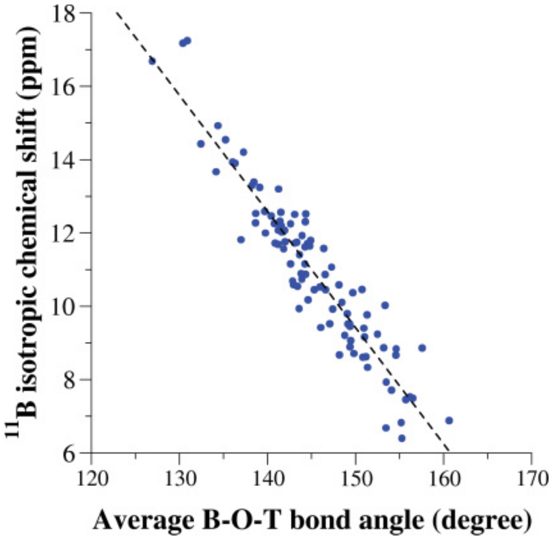

FIG. 15. (Color online) Isotropic chemical shift of trihedral boron calculated by multiple quantum magic-angle spinning (MD-GIPAW) vs the average B-O-T (where T = B or Si) bond angle (data from Ref. 25; solid line is a linear regression).

around 133°–134°. The $BO_{3\,\mathrm{nonring}}$ sites are centered around 130°–136° and correspond to boron atoms that are not part of the boroxol rings and have second-neighbor B or Si atoms (angle γ in the figure). Their angular distribution is much broader because the sites are less symmetrical.

Significant differences can be observed in the distributions of the $BO_{3\,\mathrm{ring}}$-O-(Si,B) and $BO_{3\,\mathrm{nonring}}$-O-(Si,B) contributions: when the glass is rapidly quenched, both angular distributions extend farther toward larger angles, reflecting increased disorder around these mixed [B-O-(Si,B)] sites, some of which are bound to the silicate network. The increased disorder around tricoordinate sites can already be seen in the ^{11}B MAS spectra acquired at 11.7 T (see the enlarged view of the BO_3 sites in Fig. 16). This site becomes larger and less structured as the quenching rate increases.

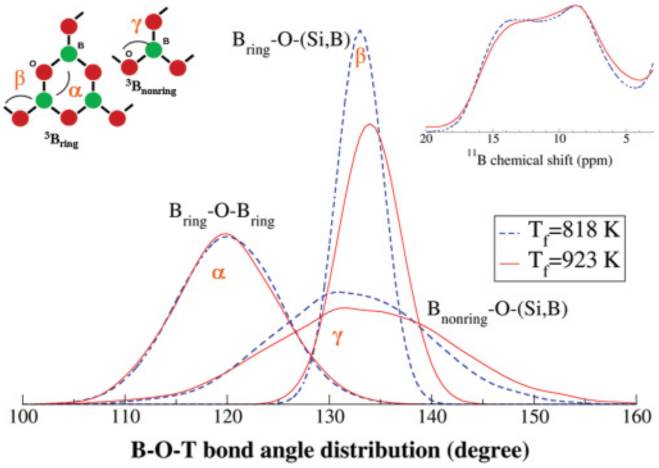

FIG. 16. (Color online) Distribution of B-O-T bond angles (T = Si, B) for trihedral boron groups in glasses A and B-1200 (insert: BO_3 sites enlarged view of the ^{11}B MAS NMR spectra).

The small differences observed for the $BO_{3\,\mathrm{ring}}$-O-$BO_{3\,\mathrm{ring}}$ contribution show that boron atoms belonging to boroxol rings, probably with fewer degrees of freedom, are unaffected. Moreover, the width of the $BO_{3\,\mathrm{ring}}$-O-$BO_{3\,\mathrm{ring}}$ distribution is of the same order of magnitude as in pure B_2O_3.[71] Similarly, we have already noted the absence of significant variations in the width of the ^{29}Si MAS lines and thus probably in the Si-O-Si angular distributions; we have recently demonstrated the sensitivity of ^{29}Si NMR to these angular distributions.[27]

Therefore, our data suggest that increasing the quenching rate results in medium-range structural disorder through the angular distributions of atoms specifically linking borate groups to silicate groups. The disorder induced by these groups may be a significant factor in the configurational contribution in borosilicate liquids. In binary alkali borates in which this type of bond is not present, most of this contribution is then related to the change in the boron coordination.

However, additional structural changes in the long-range order, not detectable by NMR and Raman spectroscopies, may also occur and contribute to the configurational contribution. A recent small-angle X-ray scattering (SAXS) measurement study suggested an increase of medium- and long-range homogeneity with an increasing fictive pressure,[72] i.e. with a decreasing fictive temperature, which has an opposite effect.[73]

V. CONCLUSION

Coupling structural investigations by NMR and Raman spectroscopy with rheological and calorimetric data provides a view of the structural impact of temperature on liquids and quenching rate on glasses. Nuclear magnetic resonance and Raman spectroscopies clearly show that the decrease in polymerization with increasing temperature is well correlated with the reduction in tetrahedral boron. These two structural parameters then follow a monotonic trend at higher temperatures. A drop of about 7% in tetrahedral boron is measured between a glass quenched at about 800 K s^{-1} and annealed, leading to a fictive temperature variation of about 100 K. Quantitative NMR measurements of boron speciation were used to calibrate the Raman spectra and thereby determine the fictive temperature of the glass directly from the boron coordination. These changes in the boron coordination account for only about 25% of the configurational heat capacity of the liquid.

The structural parameters of the melt that can account for the remaining configurational contributions were discussed in terms of the local (sodium distribution) and longer-range (angular distributions) structural data, based on ^{11}B NMR parameter distributions and a combination of molecular dynamics simulations and first-principles calculations. It has thus been shown that, although the B-O-B angular distributions of the boroxol rings (and probably the Si-O-Si distributions) are not affected by temperature, structural disorder is identified through the angular distributions of the bonds linking borate and silicate groups. This results in more broadly distributed $BO_{3\,\mathrm{ring}}$-O-(Si,B) and $BO_{3\,\mathrm{nonring}}$-O-(Si,B) angles. Also, ^{23}Na NMR showed a less homogeneous distribution of sodium atoms when the fictive temperature increases, which could favor alkali clustering when the glass has less time to be reorganized.

The structural parameter variations measured by NMR enable us to begin accounting for more parameters involved in the short- and medium-range configurational contribution of sodium borosilicate liquids. In particular, taking into account not only the boron coordination but also the alkali distribution in the network and the distribution of borate and silicate subdomains can better describe the configurational rearrangements that occur in the supercooled liquid. Applying all these approaches to a simple borosilicate glass is the first step toward a better understanding of the mechanisms responsible for the instability of liquids arising from the presence of low-solubility elements present in nuclear glass, such as the rare earth elements or molybdenum.

ACKNOWLEDGMENT

Financial support from the TGE RMN THC Fr3050 for conducting the research is gratefully acknowledged.

---

[*] Corresponding author: Dr. Frédéric Angeli, CEA Marcoule, DEN/DTCD/SECM/LCLT, BP 17171, 30207 Bagnols-sur-cze, France; frederic.angeli@cea.fr

[1] D. Caurant, P. Loiseau, O. Majérus, V. Aubin-Chevaldonnet, I. Bardez, and A. Quintas, *Glasses, Glass-Ceramics and Ceramics for Immobilization of Highly Radioactive Nuclear Wastes* (Nova Science Publishers, Hauppauge, New York, 2009), p. 359.

[2] S. Schuller, O. Pinet, and B. Penelon, J. Am. Ceram. Soc. **94**, 447 (2011).

[3] P. Richet and D. R. Neuville, in *Thermodynamic Data*, edited by S. K. Saxena (Springer-Verlag, New York, 1992), p. 132.

[4] P. K. Gupta, M. L. Lui, and P. J. Bray, J. Am. Ceram. Soc. **68**, C-82 (1985).

[5] J. F. Stebbins and S. E. Ellsworth, J. Am. Ceram. Soc **79**, 2247 (1996).

[6] T. J. Kiczenski, L. S. Du, and J. F. Stebbins, J. Non-Cryst. Solids **351**, 3571 (2005).

[7] S. Sen, J. Non-Cryst. Solids **253**, 84 (1999).

[8] S. Sen, T. Topping, P. Yu, and R. E. Youngman, Phys. Rev. B **75**, 094203 (2007).

[9] S. S. Uzun and S. Sen, J. Chem. Phys. B **111**, 9758 (2007).

[10] Wu J. and J. F. Stebbins, J. Non-Cryst. Solids **356**, 2097 (2010).

[11] K. Handa, Y. Kita, S. Kohara, K. Suzuya, T. Fukunaga, M. Misawa, T. Iida, H. Iwasaki, and N. Umesaki, J. Phys. Chem. Solids **60**, 1465 (1999).

[12] O. Majérus, L. Cormier, G. Calas, and B. Beuneu, Phys. Rev. B **67**, 024210 (2003).

[13] L. Cormier, O. Majérus, D. R. Neuville, and G. Calas, J. Am. Ceram. Soc. **89**, 13 (2006).

[14] R. Akagi, N. Ohtori, and N. Umesaki, J. Non-Cryst. Solids **293-295**, 471 (2001).

[15] T. Yano, N. Kunimine, S. Shibata, and M. Yamane, J. Non-Cryst. Solids **321**, 137 (2003).

[16] T. Yano, N. Kunimine, S. Shibata, and M. Yamane, J. Non-Cryst. Solids **321**, 147 (2003).

[17] J. F. Stebbins, Chem. Geol. **256**, 80 (2008).

[18] Y. H. Yun and P. J. Bray, J. Non-Cryst. Solids **27**, 363 (1978).

[19] S. Z. Xiao, J. Non-Cryst. Solids **45**, 29 (1981).

[20] W. J. Dell, P. J. Bray, and S. Z. Xiao, J. Non-Cryst. Solids **58**, 1 (1983).

[21] S. H. Wang and J. F. Stebbins, J. Am. Ceram. Soc. **6**, 1519 (1999).

[22] C. T. Moynihan, A. J. Easteal, M. A. DeBolt, and J. Tucker, J. Am. Ceram. Soc. **59**, 12 (1976).

[23] T. Charpentier, S. Ispas, M. Profeta, and F. Mauri, J. Phys. Chem. B **108**, 4147 (2004).

[24] T. Charpentier, P. Kroll, and F. Mauri, J. Phys. Chem. C **113**, 7917 (2009).

[25] A. Soleilhavoup, J. M. Delaye, F. Angeli, D. Caurant, and T. Charpentier, Magn. Reson. Chem. **48**, 159 (2010).

[26] F. Angeli, T. Charpentier, D. de Ligny, and C. Cailleteau, J. Am. Ceram. Soc. **93**, 2693 (2010).

[27] F. Angeli, O. Villain, S. Schuller, S. Ispas, and T. Charpentier, Geochim. Cosmochim. Acta **75**, 2453 (2011).

[28] D. Massiot, C. Bessada, J. P. Coutures, J. Virlet, and F. Tautelle, J. Magn. Reson. **90**, 231 (1990).

[29] J. P. Amoureux, C. Fernandez, and S. Steuernagel, J. Magn. Res. A **123**, 116 (1996).

[30] D. Massiot, B. Touzo, D. Trumeau, J. P. Coutures, J. Virlet, P. Florian, and P. J. Grandinetti, Solid State Nucl. Magn. Reson. **6**, 73 (1996).

[31] G. Wu, D. Rovnyak, and R. G. Griffin, J. Am. Chem. Soc. **118**, 9326 (1996).

[32] F. Angeli, T. Charpentier, M. Gaillard, and P. Jollivet, J. Non-Cryst. Solids **354**, 3713 (2008).

[33] F. H. Larsen and I. Farnan, Chem. Phys. Lett. **357**, 403 (2002).

[34] G. Czjzek, J. Fink, F. Götz, H. Schmidt, J. M. D. Coey, J. P. Rebouillat, and A. Lienard, Phys. Rev. B **23**, 2513 (1981).

[35] B. Bureau, G. Silly, J. Y. Buzare, C. Legein, and D. Massiot, Solid State Nucl. Magn. Reson. **14**, 181 (1999).

[36] N. Da, S. Krolikowski, K. H. Nielsen, J. Kaschta, and L. Wondraczek, J. Am. Ceram. Soc. **93**, 2171 (2010).

[37] Y. Yue, J. de C. Christiansen, and S. L. Jensen, Chem. Phys. Lett. **357**, 20 (2002).

[38] X. Guo, M. Potuzak, J. C. Mauro, D. C. Allan, T. J. Kiczenski, and Y. Yue, J. Non-Cryst. Solids **357**, 3230 (2011).

[39] P. Richet, Chem. Geol. **62**, 111 (1987).

[40] I. Avramov, J. Non-Cryst. Solids **238**, 6 (1998).

[41] Y. Yue, J. Non-Cryst. Solids **355**, 737 (2009).

[42] G. L. Turner, K. A. Smith, R. J. Kirkpatrick, and E. Oldfield, J. Magn. Res. **67**, 544 (1986).

[43] L. S. Du and J. F. Stebbins, Chem. Mater. **15**, 3913 (2003).

[44] L. S. Du and J. F. Stebbins, J. Phys. Chem. B **107**, 10063 (2003).

[45] G. Ferlat, T. Charpentier, A. P. Seitsonen, A. Takada, M. Lazzeri, L. Cormier, G. Calas, and F. Mauri, Phys. Rev. Lett. **101**, 065504 (2008).

[46] X. Y. Xue and J. F. Stebbins, Phys. Chem. Min. **20**, 297 (1993).

[47] A. M. George and J. F. Stebbins, Am. Miner. **80**, 878 (1995).

[48] H. Maekawa, T. Nakao, S. Shimokawa, and T. Yokokawa, Phys. Chem. Min. **24**, 53 (1997).

[49] F. Angeli, J. M. Delaye, T. Charpentier, P. Faucon, J.-C. Petit, and D. Ghaleb, J. Non-Cryst. Solids **276**, 132 (2000).

[50] T. Nanba, M. Nishimura, and Y. Miura, J. Non-Cryst. Solids **20**, 193 (1976).

[51] B. C. Bunker, D. R. Tallant, R. J. Kirkpatrick, and G. L. Turner, Phys. Chem. Glasses **31**, 30 (1990).

[52] W. L. Konijnendijk and J. M. Stevels, J. Non-Cryst. Solids **20**, 193 (1976).

[53] N. Shibata, M. Horigudhi, and T. Edahiro, J. Non-Cryst. Solids **45**, 115 (1981).

[54] B. O. Mysen, L. W. Finger, D. Virgo, and F. A. Seiffert, Am. Miner. **67**, 686 (1982).

[55] P. McMillan, Am. Miner. **69**, 622 (1984).

[56] P. Richet, Geochim. Cosmochim. Acta **48**, 471 (1984).

[57] P. Richet, J. Non-Cryst. Solids **355**, 628 (2009).

[58] G. W. Scherer, *Relaxation in Glass and Composites* (John Wiley & Sons, New York, 1986), p. 331.

[59] C. T. Moynihan, S. K. Lee, M. Tatsumisago, and T. Minami, Thermochimica Acta **280/281**, 153 (1996).

[60] G. Adam and J. H. Gibbs, J. Chem. Phys. **43**, 139 (1965).

[61] P. Richet and M. J. Toplis, C. R. Acad. Sci. Paris **t.2**, 191 (2001).

[62] P. Richet, R. A. Robie, and B. S. Hemingway, Geochim. Cosmochim. Acta **50**, 1521 (1986).

[63] M. Lenoir, A. Grandjean, Y. Linard, B. Cochain, and D. R. Neuville, Chem. Geol. **256**, 316 (2008).

[64] Y. Linard, I. Yamashita, T. Atake, J. Rogez, and P. Richet,, J. Non-Cryst. Solids **286**, 200 (2001).

[65] P. Richet, M. A. Bouhifd, P. Courtial, and C. Téqui, J. Non-Cryst. Solids **211**, 271 (1997).

[66] S. Sen, Z. Xu, and J. F. Stebbins, J. Non-Cryst. Solids **226**, 29 (1998).

[67] S. B. Liu, J. F. Stebbins, E. Schneider, and A. Pines, Geochim. Cosmochim. Acta **52**, 527 (1998).

[68] S. B. Liu, A. Pines, M. Brandriss, and J. F. Stebbins, Phys. Chem. Minerals **15**, 155 (1987).

[69] A. Abragam, *Principles of Nuclear Magnetism* (Oxford University Press, Oxford, London, 1961), p. 599.

[70] T. Charpentier, Solid State Nucl. Magn. Reson. **40**, 1 (2011).

[71] I. Hung and A. P. Howes, J. Solid. State Chem. **182**, 2402 (2009).

[72] S. Reibstein, L. Wondraczek, D. de Ligny, S. Krolikowski, S. Sirotkin, J. P. Simon, V. Martinez, and B. Champagnon, J. Chem. Phys. **134**, 204502 (2011).

[73] J. Wu, J. Deubener, J. F. Stebbins, L. Grygarova, H. Behrens, L. Wondraczek, and Y. Yue, J. Chem. Phys. **131**, 104504 (2009).